ADVANCED OPTICAL MATERIALS
www.advopticalmat.de

Phosphorescence by Trapping Defects in Boric Acid Induced by Thermal Processing

Luigi Stagi, Luca Malfatti, Alessia Zollo, Stefano Livraghi, Davide Carboni, Daniele Chiriu, Riccardo Corpino, Pier Carlo Ricci, Antonio Cappai, Carlo Maria Carbonaro, Stefano Enzo, Abbas Khaleel, Abdulmuizz Adamson, Christel Gervais, Andrea Falqui, and Plinio Innocenzi**

The phosphorescence of boric acid (BA, H_3BO_3) at room temperature is a puzzling phenomenon subject to controversial interpretations although the role of structural defects has not yet been considered. Heat treatments of boric acid cause its transformation into the metaboric phase and amorphous boron oxide (B_2O_3). The structural changes after thermal processing can create defects that become centers of luminescence and recombination channels in the visible range. In the present work, commercial boric acid is thermally processed at different temperatures. Samples treated between 200 and 400 °C exhibit remarkable phosphorescence in the visible range. At ≈480 and 528 nm, two distinct phosphorescent emissions occur, associated with trapped charge carriers recombinations identified by thermoluminescence (TL) and electron paramagnetic resonance spectroscopy (EPR). The structural and optical studies suggest that the activation of boric acid phosphorescence after heat treatment is correlated with the presence of defects. The afterglow results from a trapping and detrapping process, which delays the recombination at the active optical centers. Time-dependent density functional study (DFT) of defective BOH molecules and clusters shows the emergence of near UV and blue optical transitions in absorption. These defects trigger the photoluminescence in thermally processed boric acid samples.

1. Introduction

Hydrogen borate or boric acid is a compound of significant interest in the glass industry. It can be synthesized by reacting borax ($Na_2H_{20}B_4O_{17}$) with hydrochloric acid and typically exists in the form of colorless crystals or white powders.[1]

Upon heating at temperatures higher than 100 °C, boric acid undergoes multiple dehydration steps and ultimately forms boron oxide .[2,3] This process is accompanied by structural transformations and melting until a vitreous oxide is obtained. At room temperature (RT), this vitreous oxide may incorporate the hydroxide phase as a result of either incomplete dehydration or exposure to atmospheric aqueous vapor.[4]

Despite their wide range of potential applications, the role of boric acid and its oxide in materials obtained through heat treatment in the air or solvo/hydrothermal processing has yet to be fully understood. Recent studies have explored the use of boric acid in combination with organic compounds to create fluorescent and

L. Stagi, L. Malfatti, D. Carboni, P. Innocenzi
Laboratory of Materials Science and Nanotechnology
CR-INSTM
Department of Biomedical Sciences
University of Sassari
Viale San Pietro 43/B, Sassari 07100, Italy
E-mail: lstagi@uniss.it; plinio@uniss.it

A. Zollo, S. Livraghi
Department of Chemistry and NIS
University of Turin
Via P. Giuria 7, Turin 10125, Italy

D. Chiriu, R. Corpino, P. C. Ricci, A. Cappai, C. M. Carbonaro
Department of Physics
University of Cagliari
Sp 8, km 0.700, Monserrato, CA 09042, Italy

S. Enzo
Department of Chemical
Physics
Mathematics and Natural Sciences
University of Sassari
Via Vienna 2, Sassari 07100, Italy

A. Khaleel, A. Adamson, P. Innocenzi
College of Science
Department of Chemistry
United Arab Emirates University
Al Ain 15551, United Arab Emirates

The ORCID identification number(s) for the author(s) of this article can be found under https://doi.org/10.1002/adom.202302682

© 2023 The Authors. Advanced Optical Materials published by Wiley-VCH GmbH. This is an open access article under the terms of the Creative Commons Attribution-NonCommercial License, which permits use, distribution and reproduction in any medium, provided the original work is properly cited and is not used for commercial purposes.

DOI: 10.1002/adom.202302682

phosphorescent materials.[5–10] Boric acid, as a co-precursor in the synthesis, promotes the condensation of organic compounds into graphitic/graphene structure with enhanced fluorescence yield and significant redshift. Furthermore, when harnessed in a boric acid matrix or in polymers with boric acid, the resulting phosphors show a strong quenching-resistant fluorescence and, in some cases, a solid-state phosphorescence.[5] For instance, mixing organic precursors and boric acid can lead to the production of phosphorescent carbon dots with blue and green emissions and glowing lifetimes of 0.1-1 s after high-temperature treatment.[7,10] The main interpretation of the appearance of phosphorescence is the creation of a strong covalent boron-carbon bond along with the effective role played by the boron oxide glassy matrix in altering the vibrational and rotational characteristics of the organic moieties.[7] It is interesting to note that in all the mentioned cases the phosphorescence occurs in solid state, where the structural (crystalline or amorphous) properties of the BA matrix are preserved, without purification to remove BA species. The emission primarily falls in the blue (450 – 500 nm) and green (520–550 nm) optical regions and the excitation channels between 300 and 400 nm. The mechanism of phosphorescent recombinations is usually attributed to spin-forbidden relaxation from triplet states in a not well-defined electronic structure of the phosphors. For example, room-temperature phosphorescence (RTP) has been recently observed in commercial boric acid and attributed to recombinations from triplet states. Zheng and coworkers[11] have found that commercial boric acid powders exhibit a long afterglow in the blue region, with a maximum at 450 nm. At RT, the recombination lifetime is in the order of a tenth of a second and reaches ≈1 s at 77 K. This effect has tentatively been attributed to a weak conjugation among n electrons of O atoms in packed BA molecular units, although the simulated vertical transitions fail to indicate a possible absorption in the near ultraviolet (NUV) that is responsible for the blue phosphorescence. This explanation has been critically revised by Wu et al.,[12] who have compared the luminescence of commercial H_3BO_3 with that of trimethyl borate ($B(OMe)_3$)-derived boric acid, which is impurity-free. Under UV irradiation, they have not observed phosphorescence or optical recombination in pure boric acid although they have observed luminescence in commercial boric acid. The source of the emission in commercial samples has been associated with the existence of impurities, as the boric acid produced from $B(OMe)_3$ was free from impurities.[12] These findings suggested that, in addition to its established features, boric acid should have novel and unexplored luminescent properties with potential implications for solid-state platforms. To fully exploit these phosphorescent characteristics and effectively design phosphorescent materials, it is of paramount importance a comprehensive study of the structural properties of boron oxide and hydroxide and their inherent properties as a function of thermal processing. Investigating the properties of boric acid as a function of processing temperature up to its oxidation stage is a crucial strategy to understand the role of crystallographic phases and defects that may occur during a synthesis involving boric acid. This would enable us to discriminate the possible role of boron and its coordination with oxygen from any other interaction with a heteroatom (C, S, N, etc.) and allow the attribution of any phosphorescent properties to specific electronic states of the B-O structure.

In this work, we investigate the origin of phosphorescence in commercial boric acid treated at various temperatures. Specifically, boric acid exhibits blue and green RTP under UV light excitation when treated near the melting point. However, this RTP quenches after high-temperature treatments, which mainly result in the conversion of boric acid into boron oxide . Furthermore, the RTP can be restored by dissolving B_2O_3 in water, evaporating the water to reestablish the boric acid structure, and then retreating the material. These findings suggest that the RTP observed in boric acid arises from structural defects.

2. Results and Discussion

Commercial boric acid has been heated at various temperatures before being cooled to room temperature for characterization (**Figure 1**a). During a standard calcination process, BA powders have been placed in a ceramic crucible and subjected to heating under air atmosphere for a duration of 2 h at the selected temperature. The resulting material exhibits distinct morphological properties depending on the specific temperature employed, with BA transforming into either a coarser, grainy powder or a more densely packed vitreous solid. Within a limited range of temperatures, the treatment of pristine powders produces blue and green phosphorescent samples whose afterglow can be easily seen with the naked eye (Figure 1b).

It is well established that the crystal and amorphous structures of boric acid can vary depending on its oxidation state.[13] Thermogravimetric analysis (TGA-DSC) has been carried out over a wide temperature range to assess the relevant temperatures required to induce structural transformations. Our results show that during heating, BA undergoes distinct stages of dehydration and melting. Figure 1c shows the combined TGA and DSC analysis of H_3BO_3 performed under nitrogen flux from room temperature up to 800°C with a heating rate of 10°C • min^{-1}. Two main endothermic events are observed in the range between 80 and 200°C. The first DSC event has been recorded at 130°C and corresponds to a dehydration process of boric acid promoting the formation of the *orthorhombic metaboric acid* phase:

$$H_3BO_3 \rightarrow HBO_2 + H_2O\ (80 - 130°C) \quad (1)$$

In this range, the sample appears sintered and forms a rough bulk solid. This first process is followed by a second dehydration, where metaboric acid oxidizes into B_2O_3 (*boron trioxide*):

$$2HBO_2 \rightarrow B_2O_3 + H_2O\ (144 - 210°C) \quad (2)$$

C. Gervais
Sorbonne Université
CNRS
UMR 7574
Laboratoire de Chimie de la Matière Condensée de Paris
LCMCP
Paris F-75005, France
A. Falqui
Department of Physics "Aldo Pontremoli"
University of Milan
Via Celoria 16, Milan 20133, Italy

© 2023 The Authors. Advanced Optical Materials published by Wiley-VCH GmbH

21951071, 0, Downloaded from https://onlinelibrary.wiley.com/doi/10.1002/adom.202302682 by Universita Di Torino, Wiley Online Library on [01/12/2023]. See the Terms and Conditions (https://onlinelibrary.wiley.com/terms-and-conditions) on Wiley Online Library for rules of use; OA articles are governed by the applicable Creative Commons License

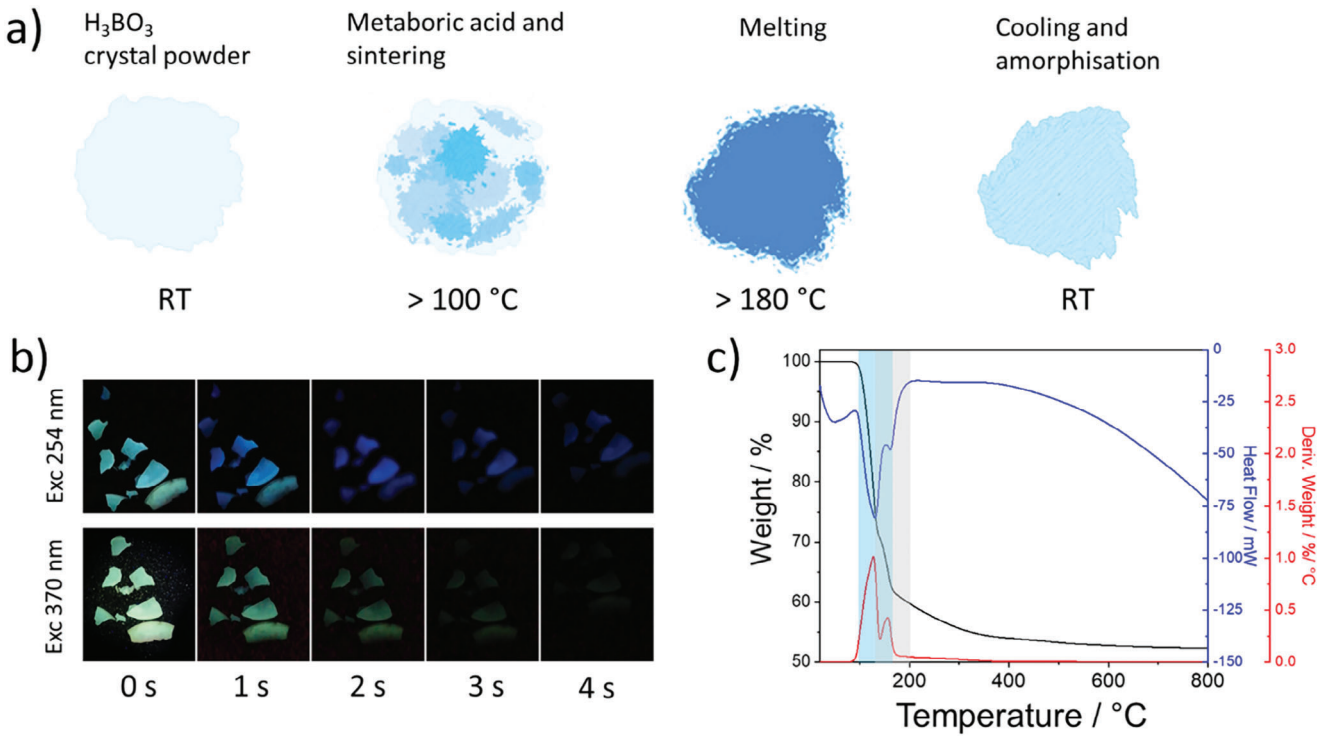

Figure 1. a) Artistic picture of boric acid thermal treatment performed in this work. b) Images of phosphorescent samples (BA250) acquired with a camera at 1 s intervals after two different excitation wavelengths; 0 s corresponds to the instant of switching off the source. c) DSC-TGA analysis of as purchased H_3BO_3. Grey and light blue areas highlight the temperature interval between the two dehydration processes.

Tetraboric acid ($H_2B_4O_7$) is assumed to occur in the second dehydration process between 180 and 200°C, although there is no clear evidence of an associated stable phase after cooling.[14]

According to TGA curves, almost 30% of weight loss is associated with the first dehydration event, while an abrupt change in slope is observed during the second one. The oxidation progresses with the temperature at a slower pace. The lack of further thermal events suggests completion of BA melting and low-rate desorption of volatile species.

In **Figure 2**a we report the XRD patterns of the as-purchased H_3BO_3 sample, and after thermal treatment in air at increasing temperatures. The samples are therefore named BA, BA100, BA130, BA200, BA300, BA400 and BA800. The H_3BO_3 diffractogram measured at RT shows a perfect match with that of crystalline boric acid (JCPDS 30–0199, sassolite). BA is characterized by $B(OH)_3$ molecules interacting by hydrogen bonds and arranged in a planar configuration (boxes in Figure 2b). The corresponding XRD pattern displays the two main reflections at 14.6° and 28.2°, which originate from (010) and (002) lattice planes. Detailed patterns are separately reported in Figure S1 (Supporting Information).

Upon heating the boric acid sample to 100 °C, it completely converts to orthorhombic metaboric acid (JCPDS 77–0425), HBO_2, with a residual H_3BO_3 (28%). However, at 130 °C, the relative amount of HBO_2 increases to 77% and reaches 87% at 200°C. After higher temperature treatments, the samples cool down in a mixture of H_3BO_3 and amorphous boron oxide. The identification of the phase composition and crystallite size has been determined using Rietveld analysis (Figure S1, Supporting Information).

Boroxol rings are interconnected by BO_3 trigonal units, as illustrated in Figure 2b. Boron oxide tends to convert into boric acid when exposed to water-absorbing conditions. This phenomenon is responsible for boron oxide instability.[4] This research has revealed a further important factor to take into account, namely a partial recrystallization of boric acid after melting.

The molecular arrangement of treated samples has been investigated by vibrational spectroscopies. Raman spectroscopy measurements in the range between 750 and 950 cm^{-1} have been reported in Figure 2b. Full spectra of pristine H_3BO_3 and BA800 are included in Figure S2 (Supporting Information). Eight vibrational modes are identifiable in boric acid under visible light excitation (λ_{exc} = 532 nm). The most intense Raman line is observed at 881 cm^{-1} and is attributed to OH bending in tetragonal BOH.[15] Some H_3BO_3 modes are still observable in BA800 in accordance with XRD data, although the most intense line is the breathing mode of boroxol rings at 807 cm^{-1}.[16] BA100 is characterized by the presence of tetragonal BOH and boroxol rings (metaboric acid structure). After increasing the temperature, the boroxol ring mode becomes predominant. Raman spectra have been collected in the temperature treatment range of 135 to 400 °C by exciting at 1064 nm to minimize fluorescence, which is still observable in BA300. Accordingly, in this interval, the samples exhibit a boroxol ring structure that can be attributed both to the metaboric acid and B_2O_3 vitreous structures. Although with

© 2023 The Authors. Advanced Optical Materials published by Wiley-VCH GmbH

21951071, 0, Downloaded from https://onlinelibrary.wiley.com/doi/10.1002/adom.202302682 by Universita Di Torino, Wiley Online Library on [01/12/2023]. See the Terms and Conditions (https://onlinelibrary.wiley.com/terms-and-conditions) on Wiley Online Library for rules of use; OA articles are governed by the applicable Creative Commons License

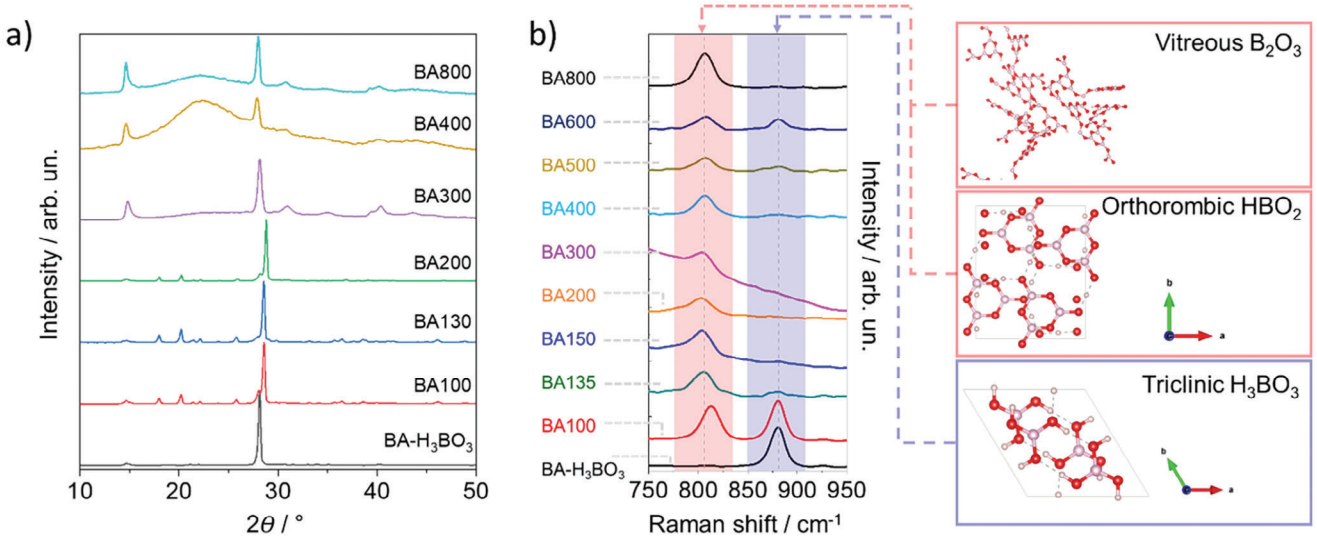

Figure 2. a) X-ray diffraction patterns of pristine H_3BO_3 powder and thermally treated BA at 100 (BA100), 130 (BA130), 200 (BA200), 300 (BA300), 400 (BA400) and 800 °C (BA800). b) Raman spectra of thermally treated BA powders in the range between 750 and 950 cm^{-1}. Characteristic OH bending in H_3BO_3 (881 cm^{-1}) and breathing mode in B_3O_3 boroxol ring (807 cm^{-1}) are highlighted. Pictures of the structural phase identified by combining XRD and Raman spectroscopy data are reported in blue and red boxes.

different occurrence, $B(OH)_3$ line at 881 cm^{-1} is always present demonstrating the partially recrystallisation as well as the conversion of oxide structure into hydroxide.[17]

Figure 3a shows the FTIR absorption spectrum of as purchased H_3BO_3 in the 4000–400 cm^{-1} range.

The most intense vibrational mode is located at 1464 cm^{-1} and corresponds to B-O stretching ν(BO). We also observe the B-O bending β(BOH) at 1192 cm^{-1} and B-O stretching ν(BOH) at 888 cm^{-1}.[15] An intense and broad absorption is recorded at 800 cm^{-1} and is attributed to B-OH out-of-plane bending β_{out}(BOH). At 640

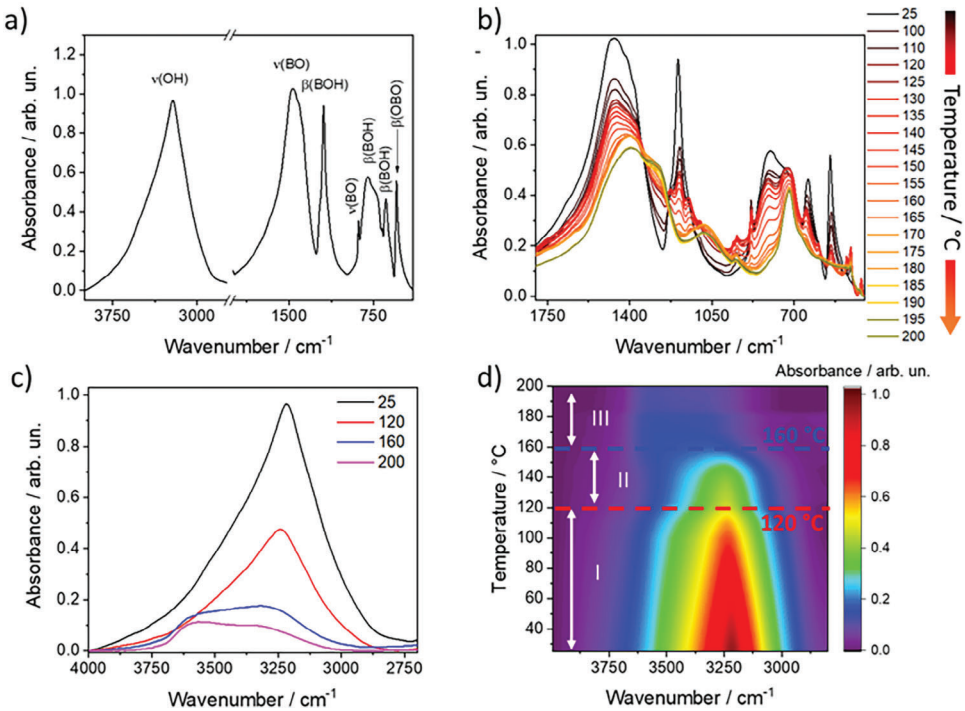

Figure 3. a) FTIR absorption spectrum of as purchased H_3BO_3 in the 4000–450 cm^{-1} range. b) FTIR absorption spectra in the 1775–950 cm^{-1} range, recorded in situ at temperatures ranging from 25 up to 200°C. c) FTIR absorption spectra in the 4000–2750 cm^{-1} range, recorded in situ at temperatures ranging from 25 up to 200 °C. d) 3D map of the FTIR spectra (2800–4000 cm^{-1}), wavenumber (*x*-axis), temperature (*y*-axis) and intensity (false color scale). The FTIR map indicates three different stages in the process, identified as I, II, and III.

© 2023 The Authors. Advanced Optical Materials published by Wiley-VCH GmbH

21951071, 0, Downloaded from https://onlinelibrary.wiley.com/doi/10.1002/adom.202302682 by Universita Di Torino, Wiley Online Library on [01/12/2023]. See the Terms and Conditions (https://onlinelibrary.wiley.com/terms-and-conditions) on Wiley Online Library for rules of use; OA articles are governed by the applicable Creative Commons License

and 540 cm^{-1} we measure a further B-OH out-of-plane bending β_{out}(BOH) and an O-B-O antisymmetric bending β(OBO).[15] The FTIR absorption spectra as a function of temperature is shown in Figure 3b. The spectra have also been recorded in situ (in KBr pellets) as a function of the temperature from 25 up to 200°C. Heat treatment of boric acid promotes a marked modulation of infrared absorption, with a broadening of the bands accompanied by a shift toward lower wavenumbers. The resulting spectrum assumes absorption characteristics detectable in numerous B_2O_3-based glasses.[18–21] We can identify at least three broad bands in the region between 2000 and 600 cm^{-1} as a result of the thermal treatment. In borate glasses, the absorption in the range 1500–1220 cm^{-1} is attributable to BO_3 stretching.[21] In particular, the two components with maxima at 1398 and 1291 cm^{-1} arise from B–O stretching vibration of borate rings and boroxol rings.[22] Small contributions from the B-O$^-$ stretching may also be present around 1520 cm^{-1}. The least intense band at 1084 cm^{-1} lies in the BO_4 stretching region of tri-, tetra-, and pentaborate groups. The third region is dominated by strong absorption at 720 cm^{-1} due to the B–O–B bending of oxygen bridges between two boron atoms, one of which is in a trigonal configuration between two boroxol ring units.[22]

The formation of an interconnected boron oxide structure proceeds with the temperature and the first change is observed ≈120–140 °C, at the beginning of the second dehydration stage when, in accordance with DSC-TGA findings, boric acid condenses into metaboric acid. Dehydration can be monitored in the 4000–2750 cm^{-1} range, which displays how the B—OH stretching mode of H_3BO_3 (3200 cm^{-1}) varies as the temperature rises (Figure 3c). At ≈160 °C, we observe a second band peaking ≈3600 cm^{-1}, partially overlapped with the 3200 cm^{-1} mode whose intensity diminishes with the increase in temperature. This band is tentatively assigned to B—OH stretching in isolated and non-hydrogen bonded OH species.[23] Boric acid at 25 °C is a well-known hydrogen-bonded solid, and the broad nature of the 3200 cm^{-1} band is due to the stretching of B—OH species in a hydrogen-bonded environment. With the proceed of dehydration and the subsequent condensation that gives boron oxide, the length of hydrogen-bonded B—OH chains decreases and more likely remains isolated B-OH, responsible for the signal at 3600 cm^{-1}. This finding can be better visualized using a 3D map of the FTIR spectra, wavenumber (x-axis), temperature (y-axis), and intensity (false color scale) (Figure 3d). Stage I, from 25 up to ≈130 °C, corresponds to the first dehydration phase; stage II is an intermediate stage where the first and second dehydrations simultaneously occur. Finally, stage III corresponds to the second dehydration with condensation and the formation of an oxide network with the production of B-OH dangling hydrogen species.

It is worth mentioning that in situ infrared analysis monitors the characteristics of the sample at a given temperature in KBr matrix. As mentioned before, the actual structure of the sample could be slightly different when cooled down at RT. This can be observed in conventional FTIR spectra at RT (Figure S3, Supporting Information). ^{11}B magic angle spinning (MAS) nuclear magnetic resonance (NMR) spectrum of boric acid (Figure S4a, Supporting Information) shows a well resolved second order quadrupolar line shape that can be fitted with parameters (δ_{iso} = 19.2 ppm; C_Q = 2.6 MHz; η_Q = 0.2) characteristic of BO_3 trigonal environment in agreement with previously reported results.[24,25] After heat-treatment at 250 °C, spectrum of BA250 sample is significantly changed: BO_3 peak remains observable, albeit with slight modifications, indicating a deviation from perfect trigonal symmetry, possibly due to factors like partial deprotonation. Furthermore, an additional narrower signal is observed at 0.5 ppm that can be assigned to the appearance of BO_4 tetragonal environment.[26] ^{1}H MAS NMR spectra of boric acid and BA250 (Figure S4b, Supporting Information) show signals centered at 8.5 and 6.7 ppm respectively, indicating modification of the proton environment during heat-treatment and possible protonation of the BO_4 sites. After higher heat-treatment, ^{11}B MAS NMR spectrum of BA800 shows only BO_3 signals and complete disappearance of BO_4 ones.

In **Figure 4** we report a summary of the optical properties of BA samples treated at different temperatures. In our experimental setup for the acquisition of steady-state photoluminescence, only samples heated to temperatures between 200 and 400 °C emit detectable luminescence. PL-PLE analysis (Figure 4a) shows that BA samples are characterized by a blue (≈410–480 nm) and a green (≈528 nm) component with a slight difference in position and intensity according to the treatment temperature. After temperature treatment at 200 °C, BA emits in the near UV-blue region with a peak at ≈410 nm (Figure 4a and 4b), excitable at 360 nm. A faint emission is also observed at ≈520 nm (Figure 4a). The temperature treatment at 250 nm enhances the green emission and redshifts the blue one. This effect is accompanied by a growth of the green component over the blue emission peaking at 460 nm. In Figure 4c, we report an example of excitation channels in the range between 250 and 500 nm for BA250 (a spectrum extended to <250 nm is reported in Figure S5, Supporting Information). Both components are excitable below 250 nm, where the band-to-band absorption tail is located. At higher wavelengths, the excitation is more selective, with maxima at 360 and 435 nm for the emissions at 480 and 528 nm, respectively. After further temperature increases to 300 and 400 °C, the 460 nm emission becomes the dominant one. In addition, the sample at 300°C appears to be the most efficient under the same experimental conditions. The emission decays in Figure 4d,e were assessed using two-exponential decays, yielding recombination lifetimes of 0.632 and 1.656 ms for the blue emission, and 0.420 and 1.278 ms for the green emission (Table S1, Supporting Information).

In accordance with previously reported findings,[27] the sample morphology changes as a result of heat treatment. The boric acid fine powder undergoes a form of sintering process characterized by larger grain sizes, compacting the sample, and causing it to firmly adhere to a substrate (Figure S6a, Supporting Information). At low processing temperatures (<200 °C), the sample is still flaky and easily reducible to a powder. At higher temperatures, the glassy appearance becomes dominant, and the sample crumbles with greater difficulty or sticks to the substrate more tightly.

In another experiment, boric acid has been placed on a silicon substrate and heated to 200 °C for 1 h. By means of Raman spectroscopy, we have detected regions with different structural properties. Point analysis exhibits regions of phase inhomogeneity, i.e., areas with a higher contribution of boroxol rings and areas with residual contributions of the $B(OH)_3$ structure. This underlines the difficulty of removing residual OH at higher temperatures (Figure S6b, Supporting Information).[28]

© 2023 The Authors. Advanced Optical Materials published by Wiley-VCH GmbH

21951071, 0, Downloaded from https://onlinelibrary.wiley.com/doi/10.1002/adom.202302682 by Universita Di Torino, Wiley Online Library on [01/12/2023]. See the Terms and Conditions (https://onlinelibrary.wiley.com/terms-and-conditions) on Wiley Online Library for rules of use; OA articles are governed by the applicable Creative Commons License

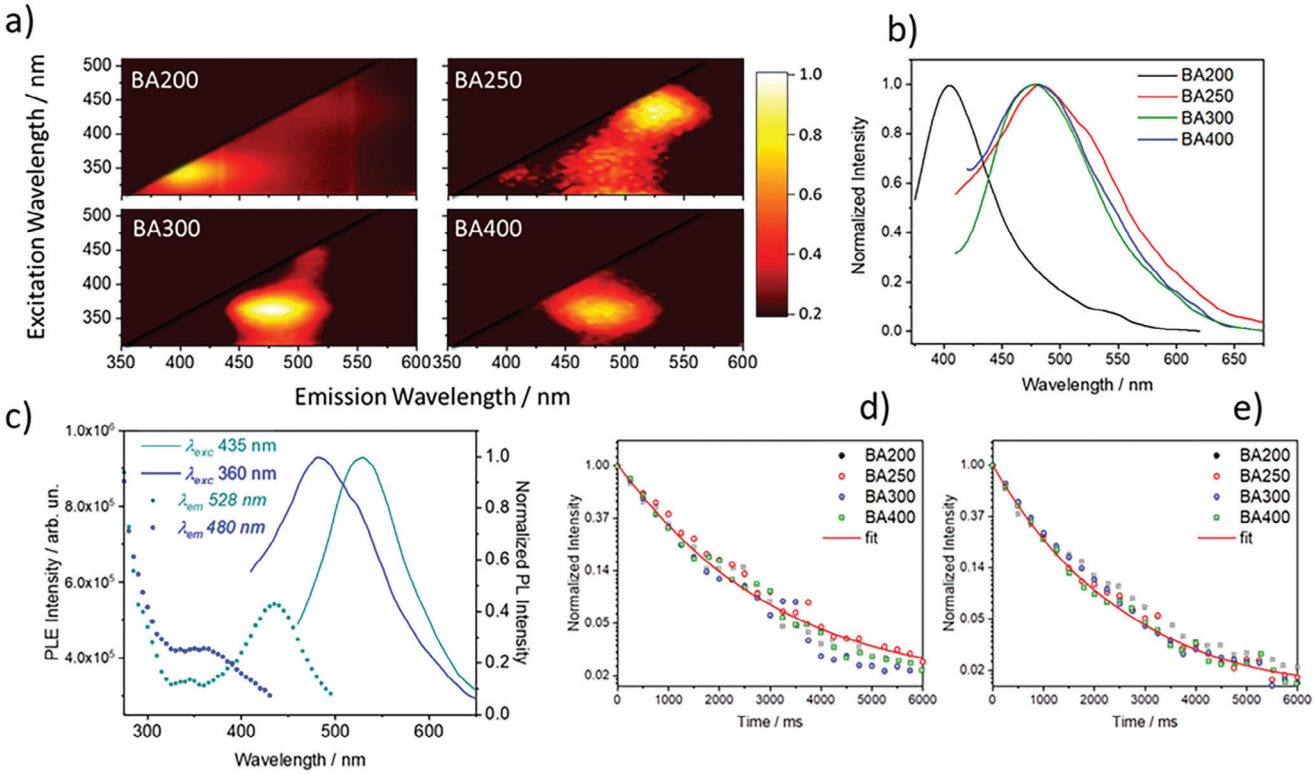

Figure 4. a) Excitation-Emission spectra (*x*-axis, emission wavelength; *y*-axis, excitation wavelength; *z*-axis, intensity emission in false colours) of BA200, BA250, BA300, and BA400. b) Normalized emission spectra under excitation at 360 nm. c) Excitation (λ_{em} = 435; 528 nm) and emission spectra (λ_{ex} = 360; 480 nm) of BA250. Time-resolved spectra of the d) blue emissions at 410 nm (BA200) and 480 nm (BA250, BA300, BA400) and e) green emissions at 528 nm (BA200, BA250, BA300, BA400).

H_3BO_3 synthesized sample (here indicated as BA-H_3BO_3*) has been obtained by reacting boron trichloride solution (BCl_3) with water and subsequently recrystallized to collect a crystalline p owder (Figure S7, Supporting Information). BA-H_3BO_3* shows identical structural and optical properties to the commercially available BA sample. Moreover, it exhibits the distinctive phosphorescence after treatment at 250 °C, confirming that this effect is inherent to boric acid and is not influenced by the specific synthesis procedure. Both commercially sourced and laboratory-synthesized samples have also been subjected to micro X-ray fluorescence analysis, confirming the absence of specific impurities introduced during synthesis and thermal processing (Figure S8, Supporting Information).

From studying the heating process of boric acid, we can summarise the general trend of B—O coordination from room temperature to 800 °C. At temperatures above 100 °C, the trigonal planar $B(OH)_3$ coordination of metaboric acid quickly converts into the trigonal HBO_2 structure with residual H_3BO_3. HBO_2 exhibits an O–B–O molecular structure in the form of boroxol rings with possible tetrahedral units coordinated to the boron atom (HBO_2(II), HBO(I)).[28,29] At higher temperatures, boroxol rings tend to arrange in disordered structures with bridging boron atoms in trigonal coordination. Based on our structural and optical measurements, the onset of phosphorescence can be correlated with the formation of boroxol rings, but it cannot be univocally assigned to a specific structural phase.

According to their electronic structures, boric acid and high-temperature-derived structures are in fact not expected to display luminescent recombination in the visible range. The electronic properties of H_3BO_3 as well as HBO_2 were investigated by DFT calculations.[30] Bulk triclinic boric acid 2A exhibits an indirect band gap of 5.98 eV. As a result of hydrogen bond-type interactions between in-plane units and van der Waals forces between out-of-plane units, the molecular nature dominates over the long-range structure. Considering the molecular orbitals, HOMO and LUMO predominantly involve OH groups.[30] Similarly, metaboric acid-based structures show a bandgap above 6 eV, and an indirect to direct gap transition is observed for the α-orthorhombic polymorph. It is also interesting to note the behavior of the orbitals involved when boroxol structures are formed. In this case, the electronic excitation originates from the p-type orbitals of the oxygen (HOMO) and then involves the π-type character of the B_3O_3 ring. This effect is shared by the orthorhombic (α-I) and monocline (β-II) structures, while the cubic (γ-III) structure has no actual participation of boron atoms in the LUCB (Lowest Unoccupied Conduction Band).[31] This evidence shows that the electronic properties of boric acid, the various polymorphs of metaboric acid, and even boron oxide in its glassy and crystalline form cannot explain the presence of radiative recombinations in the visible spectrum of any sort, fluorescence, or phosphorescence.

We hypothesize that the origin of thermally induced phosphorescence in BOH-based structures can be ascribed to structural

© 2023 The Authors. Advanced Optical Materials published by Wiley-VCH GmbH

21951071, 0, Downloaded from https://onlinelibrary.wiley.com/doi/10.1002/adom.202302682 by Universita Di Torino, Wiley Online Library on [01/12/2023]. See the Terms and Conditions (https://onlinelibrary.wiley.com/terms-and-conditions) on Wiley Online Library for rules of use; OA articles are governed by the applicable Creative Commons License

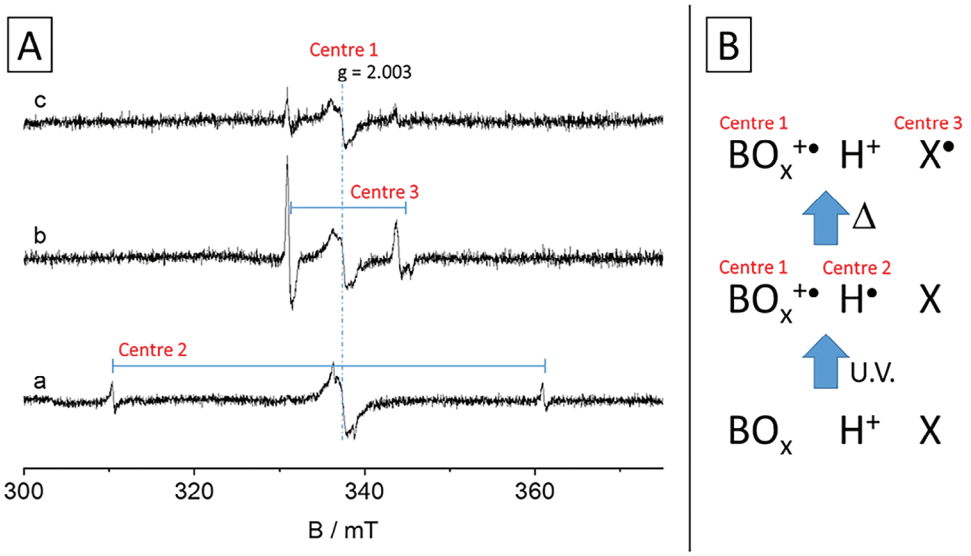

Figure 5. Panel A: EPR spectra of BA250 sample a) under UV irradiation b) after exposing the EPR cell to room temperature c) after one day at room temperature. Panel B: sketch of the processes related to the spectra evolution in panel A and involving a Boron containing structural defect (BO_x), an isolated proton and a further not assigned defect X.

defects. In addition, the sample can be treated at high temperatures to quench the phosphorescence, dissolved in water, and reprocessed until the phosphorescence emission is restored without an obvious difference, which supports the intrinsic origin of emissions.

To confirm the presence of structural defects, EPR characterization has been performed. In **Figure 5**, panel A illustrates the EPR spectra acquired at 77 K while irradiating BA250 with UV light. Upon irradiation, a distinct spectrum, labeled "*a*", emerges, revealing two discernible signals. The first signal corresponds to a paramagnetic species centered at g = 2.003 (designated as Centre 1). The spin-resonance lines appear broad and unresolved, but it is still feasible to identify spectroscopic characteristics indicative of hyperfine coupling with a boron nucleus, approximately ranging from 0.7 to 0.8 mT. (Figure S9, Supporting Information). Such a signal is compatible with boron centered radical as Boron Oxygen Hole Centres (BOHC) or Boron Electron Centres (BEC).[32] In aluminoborate glasses, BOHC defects can entrap holes on an oxygen bridging trigonal and tetragonal boron atoms. On the other hand, it is widely acknowledged that the defects in BEC defects arise from the entrapment of electrons at an unoccupied site of a nonbridging oxygen within BO_4 units.[32] Similar hyperfine coupling are also reported for borate anions impurities in calcium carbonates.[33] A second isotropic signal centered at g = 2.002 split into two components, is also detected (Centre 2). The observed splitting results from the coupling with a nucleus possessing a spin quantum number I = ½. In our context, this can be attributed exclusively to a hydrogen atom. This paramagnetic center can be identified as an isolated proton radical ($H^{\bullet}$).[34] The hyperfine coupling for this species is indeed 50.5 mT, indicating that the spin density is almost 100% localized on hydrogen nucleus as calculated from the spin density distribution formula for an *s*-type orbital ($c_s^2 = A_{iso}/A^*_{iso}$ where c_s^2 = spin density distribution, A_{iso} = isotropic splitting observed and A^*_{iso} = isotropic splitting in the free atom, 50.8 mT for the proton).[35] The process leading to the formation of this paramagnetic center is described by the first step of the sketch in Figure 5B. After turning off the lamp the two species are stable, until exposure to room temperature (spectrum *b*), after which the hydrogen radical signal disappears and simultaneously a new paramagnetic center (Centre 3) arises. The spin Hamiltonian parameters for this last species, obtained by computer simulation, are $g_{\perp} = 2.003$, $g_{//} = 1.996$ and $A_{\perp} = 12.8$ mT, $A_{//} = 13.9$ mT. The hyperfine tensor **A** indicates that also in this case a hydrogen nucleus is involved in the paramagnetic centers. However, in this case the spin density on the proton accounts for only ≈26%. The generation of this last center can be rationalized as a transfer of the spin density from the hydrogen radical to a neighboring defect (second step of the scheme in Figure 5B). Since no hyperfine coupling with boron is observable in Centre 3, it is reasonable to assign it to an oxygen-centred radical. Even after one day at room temperature, the signals persist, although they appear less intense compared to their initial intensity (spectrum *c*). If the same experiment is carried out using visible light only ($\lambda > 400$ nm) no signals are detected indicating that the observed behavior is strictly related to the UV light. Finally, it is worth mentioning that pristine H_3BO_3 sample shows a completely different behavior (Figure S10, Supporting Information). Under irradiation, only Centre 1 can be observed in pristine boric acid. This suggests that only the centers 2 and 3 have a role in the luminescence of the material. While uncertainties remain regarding the identification of the defective BO_x center, the EPR characterization undeniably reveals the existence of structural defects that respond to light irradiation, involving radical oxygens and species associated with atomic hydrogen, with a strong dependence on temperature.

The trigonal boron (BO_3) units can form the connection between boroxol rings in samples treated at higher temperatures. This configuration is also known to result from the transformation of tetrahedral boron (BO_4) to BO_3 by the formation of

© 2023 The Authors. Advanced Optical Materials published by Wiley-VCH GmbH

21951071, 0, Downloaded from https://onlinelibrary.wiley.com/doi/10.1002/adom.202302682 by Universita Di Torino, Wiley Online Library on [01/12/2023]. See the Terms and Conditions (https://onlinelibrary.wiley.com/terms-and-conditions) on Wiley Online Library for rules of use; OA articles are governed by the applicable Creative Commons License

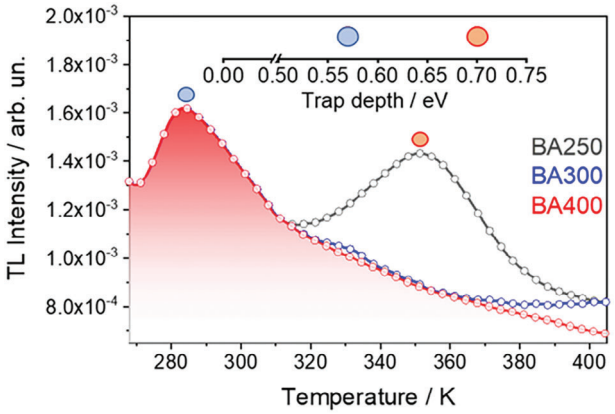

Figure 6. Thermoluminescence (TL) glow curves of BA250, BA300, and BA400 from 270 K to 400 K.

oxygen defects, specifically dangling bonds (or non-bridging oxygen (NBO)) and oxygen vacancies.[36,37]

As happens with a variety of oxides, heat treatment can promote the formation of oxygen vacancies that may, in turn, appear as neutral or charged defects.[38–41] These defects cause the formation of intragap levels in the oxide, which are responsible for absorption and emission in the near UV and visible.[42] Through EPR analysis, it has been observed that boric acid can generate additional defects in the form of radical species. These radicals can facilitate the absorption of radiation by promoting electron or trapped hole excitation.

For this reason, we have explored the presence of trapped charge carrier by structural defects in BA250, BA300, and BA400 through thermoluminescence glow curves (**Figure 6**). BA250 exhibits a TL band with maximum at 349 K, which is not detectable in BA300 and BA400. This band is correlated to intragap levels that excite low-energy green emissions, which are removed after treatment at higher temperatures (300, 400 °C). The surviving blue emissions are characterized by lower traps observed at 283 K, which are common to all samples. Our findings suggest that the characteristics blue phosphorescence of treated boric acid is correlated to trapped charged carriers, whose shallow levels are estimated to be ≈0.57 eV beneath the conduction band by the relation $E(eV) = T_m(K)/500$, where T_m is the glow peak maximum.[43] To validate this approximation, we have also applied the generalized order of kinetic model (GOK)[43] described in the supplementary materials where all the parameters found for the glow curves are reported in Table S2 (Supporting Information).

Defect sites may delay the recombination at the optical center (color centers) due to trapping and de-trapping processes. In treated samples, thermal energy can empty the traps, favoring the non-radiative recombination at the color centers. The intrinsic defects that lead to this phenomenon may involve oxygen or boron vacancies as well as unsaturated bonds. Two traps are located at 0.57 and 0.70 eV from the bottom of the conduction band. Those levels can be filled up by light excitation and eventually emptied by thermal energy. The released electron can relax without emitting radiation and recombine at the optical centers. Low energy emission disappears after thermal treatment at 300 °C, demonstrating the correlation between color centers and traps. This effect can be attributed to trap healing or structural rearrangement. Accordingly, the phosphorescence in boric acid results from delayed recombinations driven by localized trap-like defects rather than spin-prohibited transitions.[44]

Using the data obtained from the conducted experiments, we have constructed various representative structures depicting BOH coordination in different structural phases. Additionally, we have modeled probable local defects that could arise during thermal treatment, aiming to elucidate the nature of the defects referred to as BO_x in EPR investigations. The resulting optimized geometries of stable molecules and clusters have been used to predict the absorbance spectra in defective structures to be correlated with the experimental excitation spectra.[45] Structural defects can be responsible for hole and electron trapping and determine intragap energy levels in oxides.[39,40,46–48]

Due to the insulating properties and weak hydrogen bonds of boric and metaboric acid, along with the glass produced through high-temperature treatment, employing small clusters and molecules becomes a viable approach for describing the diverse structural phases and exploring the factors influencing the formation of local structural defects. In **Figure 7** we display five exemplars of molecules with the corresponding calculated absorptions. Figure 7a illustrates the experimental excitation spectra as reference for absorbing channels in treated boric acid (BA250). The first edge vertical transition in the H_3BO_3 molecular unit (Figure 7b) is located at 173.79 nm (7.1342 eV), while the strongest absorptions are at 159.13 nm (7.7916 eV; $f = 0.0261$) and 150.90 nm (8.2164 eV, $f = 0.0227$) in good accordance with already reported simulations.[11] Simulated absorption of six H_3BO_3 molecules cluster shows a slight redshift of transitions up to 153.81 nm (8.06 eV) and the absorption edge located at 164.55 (7.53 eV) nm (Figure S11, Supporting Information). However, there is no significant variation in the energy gap of the system, indicating that small clusters offer a reliable description for our specific structures. Similarly, calculated absorption in $H_3B_3O_6$ (Figure 7c) ring starts at 158.90 nm (7.8027 eV), compatible with H_3BO_3 structure. In general, although applied to simple models, the calculations support the absorption of H_3BO_3 at high energy in UV or far UV region and confirm previous reported DFT calculations on bulk boric acid and related polymorphs[30,31] indicating an indirect electronic bandgap higher than 6–7 eV. These values are a clear indication of the absence of near UV (NUV) transitions in absorption, which are supposed to trigger visible recombinations.

Defect-free bulk descriptions are inadequate to explain visible optical emissions and it is necessary to assume the formation of localized defects caused by atomic vacancies or charged molecular moieties. Figure 7d–f show three examples of defective molecular clusters as a result of hypothesized intermediate structures after dimerization and trimerization of H_3BO_3 or $H_3B_3O_6$ rings. An extended survey of other seven molecules and clusters is reported in Table S3 (Supporting Information).

According to the comparison between the theoretical absorption and the experimental spectra, bridging and non-bridging oxygen and oxygen vacancies are likely to promote UV and visible absorption in BOH structures. Figure 7d) illustrates the potential $OOBO^-$ defect as a result of a condensation of two H_3BO_3 units by dehydration process leading to the release of a water molecule. The resulting structure exhibits a non-bridging oxygen with an

© 2023 The Authors. Advanced Optical Materials published by Wiley-VCH GmbH

21951071, 0, Downloaded from https://onlinelibrary.wiley.com/doi/10.1002/adom.202302682 by Universita Di Torino, Wiley Online Library on [01/12/2023]. See the Terms and Conditions (https://onlinelibrary.wiley.com/terms-and-conditions) on Wiley Online Library for rules of use; OA articles are governed by the applicable Creative Commons License

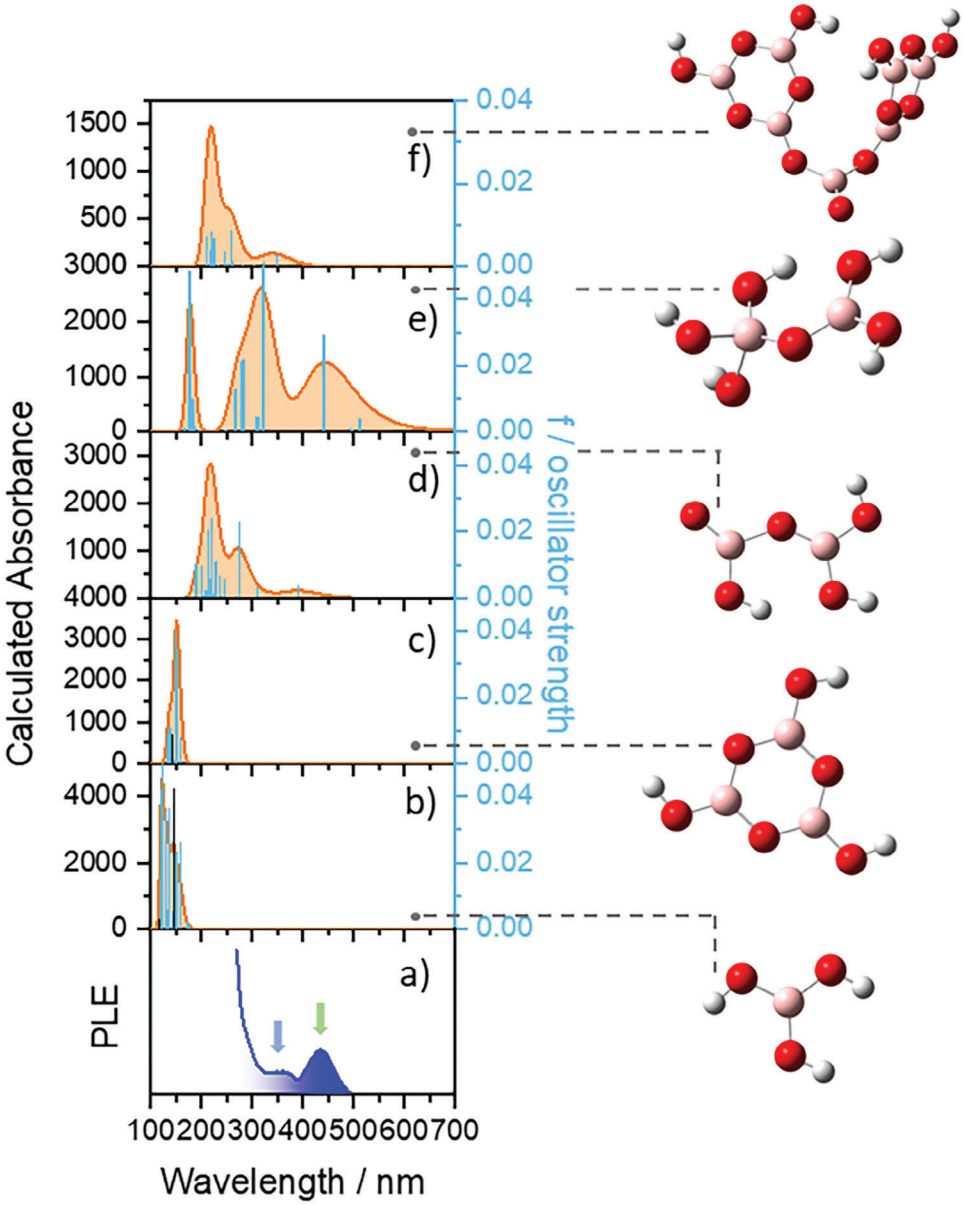

Figure 7. a) Experimental excitation bands from BA250 ($\lambda_{ex_max,1}$ = 360 nm, λ_{em_max} = 480 nm; $\lambda_{ex_max,2}$ = 435, λ_{em_max} = 528 nm and $\lambda_{ex,3}$ < 300 nm, λ_{em_max} = 480, 528 nm). b–f) calculated optical absorption and oscillator strength *f* for the five different molecules and clusters: b) H_3BO_3 ($q = 0$), c) $H_3B_3O_6$ ring ($q = 0$), d) $H_3B_2O_5$ ($q = -1$), e) $H_5B_2O_6$ ($q = 0$), f) $H_4B_7O_{13}$ ($q = -1$).

excess negative charge. The relative absorption spectrum shows a region that accurately reproduces the Urbach tail beyond 200 nm, along with an absorption band at 391.38 nm, compatible with the primary excitation channel.

Furthermore, the coordination of BO_3-BO_4 through bridging oxygen (Figure 7e) displays an absorption band at ≈321 nm and multiple transitions in the blue region of the visible spectrum, with a peak ≈440 nm, in excellent agreement with the excitation channels observed in PLE spectra. Additionally, the simulation of non-bridging oxygen in trigonal boron configuration that connects two B_3O_3 rings, as in the vitreous system, demonstrates a potential absorption at ≈350 nm, consistent with the first excitation channel. In contrast, bond saturation inhibits the NUV and visible absorption as shown in cluster 6 of Table S3 (Supporting Information). Dangling oxygens or non-bridging oxygens can absorb in the visible range with a strong dependence on the charge of the cluster, i.e., the chemical potential of the material, as demonstrated by cluster 1 and 2 in Table S3 (Supporting Information) that are able to alternatively reproduce the two excitation channels depending on their charge state.

Undercoordinated boron atoms in negatively charged cluster (BEC defect) is also responsible for the less energetic transitions that experimentally recombine by green emission (cluster 4, Table S3, Supporting Information).

In our case, there is clear experimental evidence suggesting the impossibility of measuring transitions in defect-free boric

 © 2023 The Authors. Advanced Optical Materials published by Wiley-VCH GmbH

21951071, 0, Downloaded from https://onlinelibrary.wiley.com/doi/10.1002/adom.202302682 by Universita Di Torino, Wiley Online Library on [01/12/2023]. See the Terms and Conditions (https://onlinelibrary.wiley.com/terms-and-conditions) on Wiley Online Library for rules of use; OA articles are governed by the applicable Creative Commons License

acid and boron oxide structures. Recombinations in the visible spectrum result from defects in oxygen vacancies and non-bridging oxygen. They form over a limited temperature range during heat treatment, beyond which the oxidative process tends to quench luminescence. Simulations support this hypothesis, although it would be necessary to investigate the formation of said defects at grain boundaries and during melting along with the recrystallisation process, mechanisms that complicate the theoretical study of the process. The calculated experimental excitation and absorption spectra are in agreement and indicate the possibility of triggering both phosphorescent emissions with excitation energies close to the bandgap and with selective excitation in the near UV–visible regions.

Our experiments demonstrate an important aspect of the boric acid system. The H_3BO_3 structure is unlikely to exhibit any form of fluorescence or phosphorescence in its defect-free or impurity-free form. Moreover, the optical emission mechanism in the visible range in BA and its polymorphs is not interpretable with any form of through-space conjugation (TSC) between unpaired electrons of O atoms in confined space.[49] According to our interpretation, any emission from the BOH system must be attributed to the presence of defects that may occur during the synthesis process, aging, radiation exposure, and temperature fluctuations. In this context, although we do not detect phosphorescence in our samples before thermal processing, H_3BO_3 may manifest optical emissions assuming the existence of intragap recombination centers due to defectivity. This interpretation is consistent with our study on thermal treatment, revealing the occurrence of phosphorescence within a limited temperature range during the transformation process from crystal to amorphous state, involving dehydration, bond breaking, and condensation, leading to the formation of radicals, interstitial hydrogen, and oxygen vacancies. The presence of impurities, such as metallic ions or organic molecules, could also promote the stabilization of such defects, allowing the BOH matrix to release trapped charge carriers, inducing the phenomenon of phosphorescence in hybrid systems.

3. Conclusion

Heating boric acid to temperatures near or above its melting point results in structural defects that exhibit a phosphorescence when exposed to UV and visible light. Phosphorescence lasting hundreds of microseconds has been correlated to structural changes caused by a rise in temperature, specifically the transition to metaboric acid and boron oxide. In addition, the emission is characterized by two UV and visible excitation channels that relax in the blue and green regions, respectively.

The experimental results do not support the hypothesis that conventional spin-forbidden recombinations in stoichiometric material or impurities are the source of phosphorescence in boric acid. Delayed recombination in the presence of defective material is in better accordance with the experimental results. The blue and green optical centers are compatible with the formation of structural defects of oxygen vacancies and unsaturated bonds. They are formed during the melting and recrystallisation process and reduce their occurrence by treatment at higher temperatures, where the oxide phase is predominant. The possibility of engineering defects as color centers in boric acid opens up new scenarios for the development of novel room-temperature phosphorescent materials.

Supporting Information

Supporting Information is available from the Wiley Online Library or from the author.

Acknowledgements

L.S. acknowledges the Italian Ministry for Research and Education (MUR) for the financial support.

Conflict of Interest

The authors declare no conflict of interest.

Author Contributions

L.S. designed methodology; conceptualized the idea for study; performed visualization; wrote the original draft; performed investigation and formal analysis; and also writing, reviewed, and edited the final manuscript. L.M., S.E., and A.F. performed formal analysis. A.Z., S.L., D.C., R.C., P.C.R., A.C., and C.M.C. formal analysis and investigation. D.C. performed Investigation. A.K. and A.A. performed Investigation. P.I. performed formal analysis; wrote and reviewed the manuscript. All authors have read and agreed to the submitted version of the manuscript.

Data Availability Statement

The data that support the findings of this study are available from the corresponding author upon reasonable request.

Keywords

borates, boric acid, defects, electron traps, phosphorescence

Received: October 21, 2023
Published online:

[1] A. Mergen, M. H. Demirhan, M. Bilen, *Adv. Powder Technol.* **2003**, *14*, 279.
[2] P. Wang, J. J. Kosinski, M. M. Lencka, A. Anderko, R. D. Springer, *Pure Appl. Chem.* **2013**, *85*, 2117.
[3] G. Kaur, S. Kainth, R. Kumar, P. Sharma, O. P. Pandey, *React. Kinet., Mech. Catal.* **2021**, *134*, 347.
[4] E. Mccalla, R. Brüning, *J. Mater. Res.* **2002**, *17*, 3098.
[5] J. Ren, L. Stagi, P. Innocenzi, *Prog. Solid State Chem.* **2021**, *62*, 100295.
[6] R.-S. Juang, C.-T. Hsieh, C.-P. Kao, Y. A. Gandomi, C.-C. Fu, S.-H. Liu, S. Gu, *Carbon N Y* **2021**, *176*, 61.
[7] D. Wang, Z. Lu, X. Qin, Z. Zhang, Y. Shi, J. W. Y. Lam, Z. Wang, B. Z. Tang, *Adv. Opt. Mater.* **2022**, *10*, 1.
[8] A. B. Bourlinos, G. Trivizas, M. A. Karakassides, M. Baikousi, A. Kouloumpis, D. Gournis, A. Bakandritsos, K. Hola, O. Kozak, R. Zboril, I. Papagiannouli, P. Aloukos, S. Couris, *Carbon N Y* **2015**, *83*, 173.

© 2023 The Authors. Advanced Optical Materials published by Wiley-VCH GmbH

21951071, 0, Downloaded from https://onlinelibrary.wiley.com/doi/10.1002/adom.202302682 by Universita Di Torino, Wiley Online Library on [01/12/2023]. See the Terms and Conditions (https://onlinelibrary.wiley.com/terms-and-conditions) on Wiley Online Library for rules of use; OA articles are governed by the applicable Creative Commons License

[9] X. Zheng, Y. Huang, W. Lv, J. Fan, Q. Ling, Z. Lin, *Angew. Chem., Int. Ed.* **2022**, *61*, e202207104.
[10] W. Li, W. Zhou, Z. Zhou, H. Zhang, X. Zhang, J. Zhuang, Y. Liu, B. Lei, C. Hu, *Angew. Chem., Int. Ed.* **2019**, *58*, 7278.
[11] H. Zheng, P. Cao, Y. Wang, X. Lu, P. Wu, *Angew. Chem., Int. Ed.* **2021**, *60*, 9500.
[12] Z. Wu, J. C. Roldao, F. Rauch, A. Friedrich, M. Ferger, F. Würthner, J. Gierschner, T. B. Marder, *Angew. Chem., Int. Ed.* **2022**, *61*, e202200599.
[13] F. Sevim, F. Demir, M. Bilen, H. Okur, *Korean J. Chem. Eng.* **2006**, *23*, 736.
[14] S. Aghili, M. Panjepour, M. Meratian, *J. Therm. Anal. Calorim.* **2018**, *131*, 2443.
[15] M. Bezerra Da Silva, R. C. R. Santos, P. T. C. Freire, E. W. S. Caetano, V. N. Freire, *J. Phys. Chem. A* **2018**, *122*, 1312.
[16] J. L. Parsons, *J. Chem. Phys.* **1960**, *33*, 1860.
[17] G. E. Walrafen, S. R. Samanta, P. N. Krishnan, *J. Chem. Phys.* **1980**, *72*, 113.
[18] C. Julien, M. Massot, W. Balkanski, A. Krol, W. Nazarewicz, *Mater. Sci. Eng. B* **1989**, *3*, 307.
[19] P. Umari, A. Pasquarello, *Phys. Rev. Lett.* **2005**, *95*, 6.
[20] D. Möncke, G. Tricot, A. Winterstein-Beckmann, L. Wondraczek, E. I. Kamitsos, *Phys. Chem. Glas. Eur. J. Glas. Sci. Technol. Part B* **2015**, *56*, 203.
[21] H. A. Othman, H. S. Elkholy, I. Z. Hager, *J. Mol. Struct.* **2016**, *1106*, 286.
[22] E. I. Kamitsos, M. A. Karakassides, G. D. Chryssikos, *J. Phys. Chem.* **1987**, *91*, 1073.
[23] C. E. Weir, *J. Res. Natl. Bur. Stand. Sect. A Phys. Chem.* **1966**, *70A*, 153.
[24] A. D. Irwin, J. S. Holmgren, J. Jonas, *J Non Cryst Solids* **1988**, *101*, 249.
[25] G. D. Sorarù, N. Dallabona, C. Gervais, F. Babonneau, *Chem. Mater.* **1999**, *11*, 910.
[26] J. F. Stebbins, P. Zhao, S. Kroeker, *Solid State Nucl. Magn. Reson.* **2000**, *16*, 9.
[27] C. Huber, S. S. Jahromy, F. Birkelbach, J. Weber, C. Jordan, M. Schreiner, M. Harasek, F. Winter, *Energy Sci. Eng.* **2020**, *8*, 1650.
[28] D. M. Schubert, in *Ullmann's Encyclopedia of Industrial Chemistry*, **2015**, pp. 1–32, https://doi.org/10.1002/14356007.a04_263.pub2.
[29] C. C. Freyhardt, M. Wiebcke, J. Felsche, *Acta Crystallogr.* **2000**, *56*, 276.
[30] M. B. Da Silva, R. C. R. Dos Santos, A. M. Da Cunha, A. Valentini, O. D. L. Pessoa, E. W. S. Caetano, V. N. Freire, *Cryst. Growth Des.* **2016**, *16*, 6631.
[31] M. B. Da Silva, A. M. Da Cunha, R. C. R. Santos, A. Valentini, E. W. S. Caetano, V. N. Freire, *New J. Chem.* **2017**, *41*, 15533.
[32] W. M. Pontuschka, S. Isotani, A. Piccini, *J. Am. Ceram. Soc.* **1987**, *70*, 59.
[33] R. S. Eachus, M. C. R. Symons, *J. Chem. Sci. A* **1968**, 2438.
[34] P. J. Angiolillo, J. M. Vanderkooi, *Photochem. Photobiol.* **1996**, *64*, 492.
[35] J. A. J. Fitzpatrick, F. R. Manby, C. M. Western, *J. Chem. Phys.* **2005**, *122*, 084312.
[36] L. Skuja, *J. Alloys Compd.* **1996**, *239*, 16.
[37] F. A. Abdel-Wahab, A. M. Fayad, M. Abdel-Baki, H. Abdelmaksoud, *J. Non Cryst. Solids* **2018**, *500*, 84.
[38] I. N. Ogorodnikov, L. I. Isaenko, A. V. Kruzhalov, A. V. Porotnikov, *Radiat. Meas.* **2001**, *33*, 577.
[39] S. Mukhopadhyay, P. V. Sushko, A. M. Stoneham, A. L. Shluger, *Phys Rev B Condens Matter Mater Phys* **2004**, *70*, 195203.
[40] P. V. Sushko, S. Mukhopadhyay, A. M. Stoneham, A. L. Shluger, *Microelectron. Eng.* **2005**, *80*, 292.
[41] C. Linderälv, D. Åberg, P. Erhart, *Chem. Mater.* **2021**, *33*, 73.
[42] A. Shyichuk, E. Zych, *J. Phys. Chem. C* **2020**, *124*, 14945.
[43] A. J. J. Bos, *Materials* **2017**, *10*, 1357.
[44] F. Clabau, X. Rocquefelte, T. Le Mercier, P. Deniard, S. Jobic, M.-H. Whangbo, *Chem. Mater.* **2006**, *18*, 3212.
[45] J. Ren, L. Stagi, C. M. Carbonaro, L. Malfatti, M. F. Casula, P. C. Ricci, A. E. Del Rio Castillo, F. Bonaccorso, L. Calvillo, G. Granozzi, P. Innocenzi, *2D Mater.* **2020**, *7*, 045023.
[46] T. Zhang, A. Solé-Daura, S. Hostachy, S. Blanchard, C. Paris, Y. Li, J. J. Carbó, J. M. Poblet, A. Proust, G. Guillemot, *J. Am. Chem. Soc.* **2018**, *140*, 14903.
[47] A. Paleari, F. Meinardi, S. Brovelli, R. Lorenzi, *Commun. Phys.* **2018**, *1*, 67.
[48] M. Sachs, J.-S. Park, E. Pastor, A. Kafizas, A. A. Wilson, L. Francàs, S. Gul, M. Ling, C. Blackman, J. Yano, A. Walsh, J. R. Durrant, *Chem. Sci.* **2019**, *10*, 5667.
[49] Z. Zhang, Z. Wang, X. Liu, Y. Shi, Z. Li, Y. Zhao, *Adv. Sci.* **2023**, *10*, 1.

© 2023 The Authors. Advanced Optical Materials published by Wiley-VCH GmbH

21951071, 0, Downloaded from https://onlinelibrary.wiley.com/doi/10.1002/adom.202302682 by Universita Di Torino, Wiley Online Library on [01/12/2023]. See the Terms and Conditions (https://onlinelibrary.wiley.com/terms-and-conditions) on Wiley Online Library for rules of use; OA articles are governed by the applicable Creative Commons License